Air-Bridge Integrated Slot-Ring Antennas for HEB Devices: New Fabrication Techniques*

Dazhen Gu, Eyal Gerecht, Xin Zhao, and Sigfrid Yngvesson

Abstract—In order to develop multi-pixel focal plane arrays at terahertz frequencies based on hot electron bolometer (HEB) technology, special consideration must be given to the power coupling configuration. Tunable terahertz local oscillator (LO) sources have insufficient power to bias large arrays of HEB mixers. We are developing a new quasi-optical coupling structure consisting of a slot-ring antenna and an elliptical silicon lens. The goal of the project is to eliminate the need for a beam splitter or diplexer and to couple both LO beam and signal beam directly to the antenna. This direct coupling can be achieved by setting the polarizations of the LO and signal beams to be orthogonal to each other. The IF power is extracted through a coplanar waveguide (CPW) that includes a stub filter to prevent the loss of terahertz power from the slot-ring. Discontinuities in the CPW structure cause even symmetry modes to propagate. An air-bridge ground plane structure can prevent the propagation of such undesirable modes, through which terahertz and IF power may be lost. Although slot-ring antennas, including air-bridges, have been used successfully at much lower frequencies, they present a fabrication and design challenge at terahertz frequencies. We have developed a complex fabrication technique for the construction of HEB devices at the terminals of air-bridge integrated slot-ring antennas.

Index Terms— HEB devices, quasi-optical coupling, slot-ring antenna, terahertz receivers.

I. INTRODUCTION

TERAHERTZ radiation, with frequencies between those of millimeter waves and the infrared, exhibits unique properties for radio astronomy, biomedical, and homeland security applications. A number of terahertz technologies for use in imaging, remote sensing, and spectroscopy, are under development [1-5]. All these applications rely on reliable terahertz sources that can provide sufficient power and high tunability. The main terahertz source technologies are listed below.

A. Far-infrared Lasers

Far-infrared (FIR) lasers consist of a tunable Fabry-Perot cavity optically pumped by a continuous wave carbon dioxide (CO_2) laser [6]. Optically pumped lasers can operate at many frequencies, which fully cover the terahertz range (from 300 GHz to 10 THz). FIR lasers are used primarily only in laboratory research because of their bulky size and difficulty of operation. Although there are many spectral lines corresponding to different frequencies of operation, FIR lasers lack sufficient tunability. A custom-designed FIR laser system, under operation at the UMass Terahertz Laboratory, is shown in Fig. 1(a).

B. Harmonic Multipliers

Harmonic multipliers have been widely used in RF circuits from megahertz frequencies to gigahertz frequencies. Recent development of Gallium Arsenide (GaAs) Schottky diode harmonic multipliers has pushed this technology into the terahertz regime. Driven by millimeter wave synthesizers, harmonic multipliers can directly multiply the frequency up to terahertz frequencies. However, the available output power from harmonic multipliers decreases with increasing frequency. The best harmonic multiplier source at about 700 GHz can generate one hundred microwatts of output power, which is barley sufficient to provide biasing power for a small number of detectors, but insufficient for focal plane arrays with a medium or large number of detectors. Harmonic multiplier sources generate less than 10 µW at frequencies above 1 THz but have a significant advantage over other terahertz sources in terms of their size (very mobile), ease of use, and tunability. Fig. 1(b) shows a commercially available multiplier source.
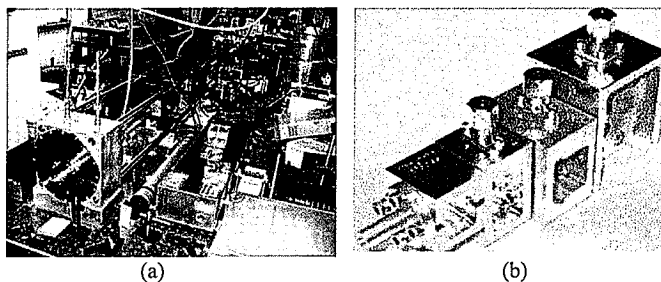

(a)   (b)

Fig. 1. Terahertz sources: (a) far-infrared laser; (b) harmonic multiplier.

C. Quantum Cascade Lasers

Quantum cascade lasers (QCL), invented by scientists at Bell Labs for optical wavelengths, are under development at terahertz frequencies [7]. QCLs usually consist of so-called quantum wells which include a few hundred molecular beam epitaxy (MBE) grown layers of nanometer-thin alloy materials, such as gallium and aluminum compounds. These quantum wells are arranged in a QCL device as a waterfall structure with each layer at a lower energy level than the one before. When an electric current flows through a QCL device, the electrons jump from one energy level to another, rather than moving smoothly between levels, and similarly the electrons tunnel from one layer to the next going "through" rather than "over" energy barriers separating the wells. This cascading effect produces sufficient gain in the QCL. The frequency of the QCL can be tuned by adjusting the thickness of the layers. Although QCLs have become a well-established radiation source technology for the mid-infrared region, the output power level at frequencies lower than 3 THz is still very small. QCLs operate at cryogenic temperatures, and temperature instability will result in a frequency shift. QCLs are not currently commercially available.

Harmonic multiplier sources are the most promising technology for mobile terahertz imagers. A two-dimensional terahertz imaging system employing a harmonic multiplier source is under development at the National Institute of Standards and Technology in collaboration with the UMass Terahertz Laboratory.

To efficiently utilize the power from a multiplier source at terahertz frequencies, we developed a quasi-optical design based on a slot-ring antenna and an elliptical silicon lens. The LO injection scheme, shown in Fig. 2, will be used to pump the state-of-the-art hot electron bolometer (HEB) mixers. By fabricating the HEB device at a location of 45 degrees with respect to the slot input, the polarizations of LO and signal beams can be set orthogonal to each other. The signals are then combined using a wire grid instead of a beam splitter. In order to eliminate the spurious slot-line mode propagating through the IF channel, an air-bridge structure is required to be integrated with the slot-ring antenna. The small dimensions of the slot-ring antenna at terahertz frequencies require a new fabrication process. This paper describes the design of an air-bridge integrated slot-ring antenna and the new fabrication process for such structures.

II. ANTENNA AND FILTER DESIGN

Slot-ring antennas have been used in millimeter-wave receivers with balanced mixer configurations [8][9]. When these structures are used for sub-millimeter-wave applications, the power loss due to substrate modes becomes increasingly important. A convenient way to eliminate substrate modes is to place the slot-ring antenna substrate on a dielectric lens having roughly the same dielectric constant [10]. The lens acts as an
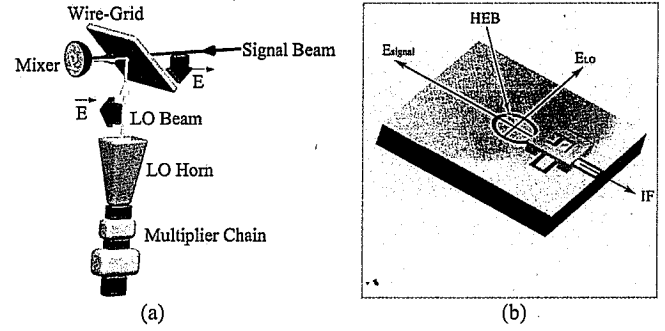

Fig. 2. (a) LO injection scheme; (b) slot-ring antenna with an air-bridge design.

effective dielectric half-space. Most of the power (about 97 %) radiates into the dielectric half-space. The power radiating outwards into the vacuum side (3 %) contributes 0.1 dB to the total system noise figure [11]. The design of a slot-ring antenna with a resonance frequency centered at 1.56 THz was reported in a previous publication [12]. The impedance of the antenna, with a ring radius of 13.5 μm and a slot width of 2 μm, was simulated to be 90 Ω. In the following subsections, theoretical calculations of the radiation pattern of the slot-ring antenna and S-parameters of the stub filter are discussed.

A. Radiation Pattern of Slot-ring Antenna with Lens

In order to obtain the radiation pattern of the slot-ring antenna on a silicon lens, we first calculate the far-fields of the antenna without the presence of the lens, and then add the effects of the lens. At the resonance frequency, the circumference of the slot-ring is close to one guided wavelength ($1.07\lambda_g$). The magnitude of the electric field in the slot has a sinusoid distribution and varies only along the azimuthal angle. Therefore, the slot-ring can be equivalently viewed as a magnetic current loop with its magnitude given by

$$M(\varphi) = M_0 \cos(ka\varphi), \qquad (1)$$

where k is the propagation constant, a is the radius of the slot-ring, and φ is the azimuthal angle. The aperture radiation pattern can be calculated from the effective magnetic and electric current densities [13]. Starting from Eq. (1), we can derive the far-field radiation pattern as

$$E_\theta(\theta,\varphi) \sim J_1'(ka \cdot \sin\theta) \cdot \cos\varphi \text{ and} \qquad (2)$$

$$E_\varphi(\theta,\varphi) \sim \frac{J_1(ka \cdot \sin\theta)}{ka \cdot \sin\theta} \cdot \cos\theta \cdot \sin\varphi, \qquad (3)$$

where $k=k_d=2\pi/\lambda_d$ for the dielectric side and $k=k_0=2\pi/\lambda_0$ for the vacuum side, J_1 is the first order Bessel function of the first kind and J_1' is its first derivative.

The silicon lens functions as a beam-focusing element, and hence will reshape the far-field radiation pattern. We used a ray-optics approach and a two-dimensional Fourier transform to include the effects of the lens [14]. At the interface between

the dielectric lens and the vacuum, the field components in spherical coordinate system are transformed to the cylindrical coordinate system (see Fig. 3). On the dielectric side, it is convenient to use the spherical coordinate system for a point source, which is the slot-ring antenna. In order to calculate the far-field pattern, we need to integrate the electromagnetic fields on the two dimensional plane just outside of the dielectric lens. This requires us to use a cylindrical coordinate system on the vacuum side. The electric fields of the point source (E_θ and E_φ) are therefore transformed to the fields on the plane (E_ρ and E_φ) as follows:

$$E_\rho'(\rho,\varphi') = E_\theta(\theta',\varphi') \cdot \frac{n - \cos\theta'}{(n-1)f} t_\theta \cdot \frac{1}{r} \text{ and} \quad (4)$$

$$E_\varphi'(\rho,\varphi') = E_\varphi(\theta',\varphi') \cdot \frac{n - \cos\theta'}{(n-1)f} t_\varphi \cdot \frac{1}{r}, \quad (5)$$

where f is the distance from the slot-ring antenna to the top of the lens, n is the dielectric constant of the silicon lens, and t_θ and t_φ are the field transmission coefficients through the interface between the lens and the vacuum half-space. Subscripts θ and φ correspond respectively to the elevational and azimuthal directions.

In terms of the far-field radiation, we are concerned about the relative pattern rather than the absolute value. Eq. (4) and Eq. (5) are then simplified as follows:

$$E_\rho'(\theta',\varphi') \sim J_1'(ka \cdot \sin\theta') \cdot \cos\varphi' \cdot t_\theta \cdot \frac{1}{r} \text{ and} \quad (6)$$

$$E_\varphi'(\theta',\varphi') \sim \frac{J_1(ka \cdot \sin\theta')}{ka \cdot \sin\theta'} \cdot \cos\theta' \cdot \sin\varphi' \cdot t_\varphi \cdot \frac{1}{r}. \quad (7)$$

The final far-field pattern can be obtained by integrating on the closed surface, just outside of the lens (s'). The electrical fields, E_θ and E_φ, are then expressed as follows:
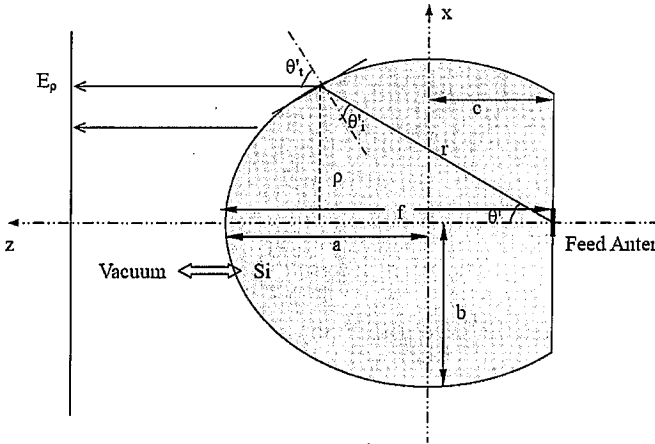
$$E_\theta \sim (1 + \cos\theta) \iint_{s'} [E_\varphi' \sin(\varphi - \varphi') + E_\rho' \cos(\varphi - \varphi')] \\ \cdot e^{jk\rho \sin\theta \cos(\varphi-\varphi')} \rho \cdot d\rho d\varphi' \quad (8)$$

$$E_\varphi \sim (1 + \cos\theta) \iint_{s'} [E_\varphi' \cos(\varphi - \varphi') - E_\rho' \sin(\varphi - \varphi')] \\ \cdot e^{jk\rho \sin\theta \cos(\varphi-\varphi')} \rho \cdot d\rho \cdot d\varphi'. \quad (9)$$

The terms of E_ρ' and E_φ' in Eq. (8) and Eq. (9) can be substituted by Eq. (6) and Eq. (7).

Fig. 4 shows the far-field radiation patterns as calculated from Eq. (8) and Eq. (9). The beam in the H-plane is slightly wider than the one in the E-plane and therefore agrees with the results obtained by [8]. The simulated side lobe levels (SLLs) of 15.7 dB in the E-plane and 19.7 dB in the H-plane are also similar to the results of [8]. Another important characteristic of the radiation pattern is the 3 dB beamwidth of the main lobe. The 3dB beamwidth of the main lobe is less than 3° for both the E-plane and the H-plane (see Fig. 4).

B. Performance of Bandstop Filter with Air-bridge

We chose a double-stub bandstop filter because of its advantages of being less prone to picking up RF/LO radiation. Two quarter-wavelength long open-circuit stubs are placed one quarter-wavelength away from the slot-ring antenna and form the bandstop filter. The open-circuit is therefore transformed to the interface between the CPW and the slot-ring antenna. Such filters introduce even-symmetry modes of propagation due to discontinuities in the CPW structure. These even modes can cause extra loss to the LO and the RF, resulting in higher LO power requirements as well as a higher receiver noise temperature. In order to suppress the undesirable modes, an air-bridge structure is fabricated on top of the double-stubs to form an elevated ground plane.

A number of simulations were performed to study the performance of the double-stub filter and then optimize its dimensions. Fig. 5 shows the simulation results of the bandstop

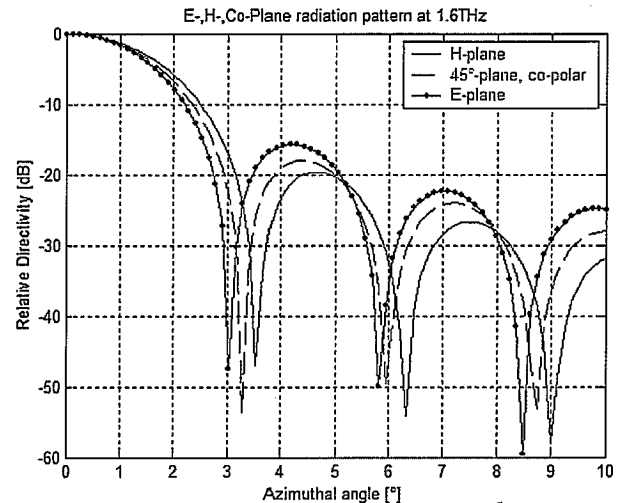Fig. 3. Illustration of a silicon lens as a beam reshaping element.

Fig. 4. Far-field radiation pattern of the lens-integrated, slot-ring antenna.
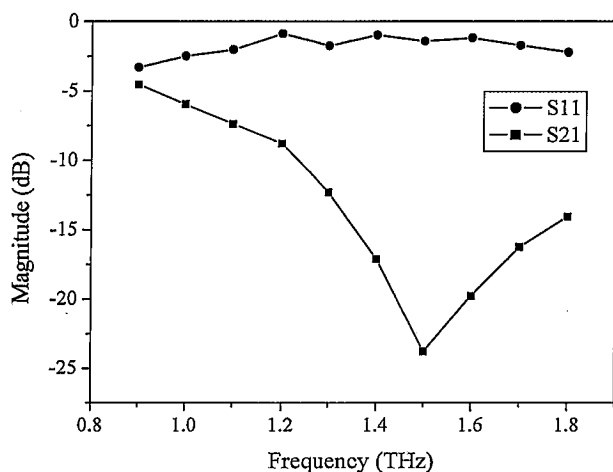
Fig. 5. Simulation results of the air-bridge integrated stub filter.

Fig. 6. Illustration of the HEB device fabrication steps.

filter S-parameters. The insertion loss (S_{21}) at the center frequency (1.5 THz) is about 25 dB. The insertion loss without the air-bridge structure is less than 15 dB at the center frequency. This 10 dB difference in the insertion loss demonstrates the effectiveness of the air-bridge structure.

III. FABRICATION PROCESS

HEB devices were fabricated on a NbN film 3.5 nm thick, that was deposited on a silicon substrate by DC magnetron sputtering. The active region of the NbN strip is 4 μm wide by 0.5 μm long. Fig. 6 shows the main steps of the fabrication process. We fabricated the device using an advanced stepper lithography instrument. Such a system utilizes ultra-short (365 nm wavelength) UV light to reduce diffraction and thus achieve higher resolution. Furthermore, the stepper instrument contains lenses of high numerical aperture designed to project the exposure light with a reduction of image size on the wafer by a factor of five. We have also introduced a bi-level lift-off process that improves the yield of the critical submicron lift-off step. In addition to the standard photoresist, the chip is first coated with a layer of MicroChem [15] lift-off resist (LOR). At a specific pre-bake temperature, the LOR layer produces a sideways undercut distance of 0.1 to 0.2 μm, which ensures good lift-off with thin film edge quality without flakes or fences.

After the metallization and lift-off steps, a strip of photo resist was patterned on the device in order to protect it from the reactive ion etch (RIE) process. This step is designed to remove the excess NbN film.

Next, a backside alignment window for the lens positioning was patterned. This step was performed using a standard contact aligner and an infrared camera for aligning the window on the back side of the silicon substrate. After the titanium-gold layer was deposited on the chip in an E-beam evaporation chamber, an additional lift-off step was performed to open the window.

Once the fabrication of the device was completed, the air-bridge was constructed. Fig. 7 illustrates the two main steps
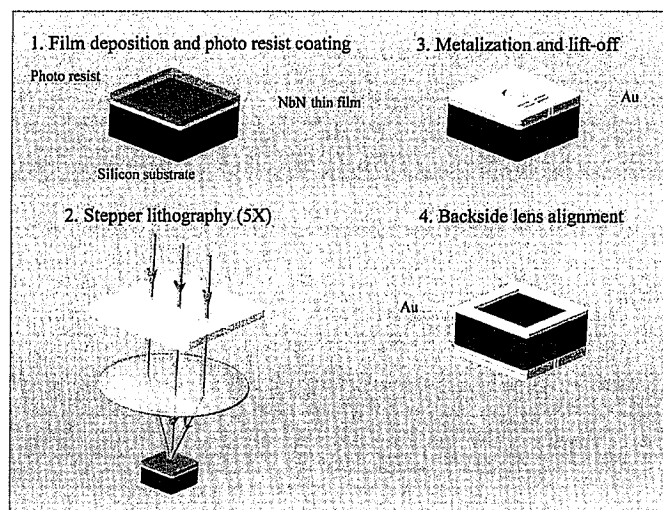
involved in the fabrication of the air bridge structure. The air-bridge structure, which consists of 6 μm tall posts and 3 μm thick spans, was constructed by a gold electroplating process. This step was carried out by use of a commercially-available noncyanide electrolytic solution (TECHNI-GOLD 25 MAKEUP ES [15]) at a temperature of 60 °C. The thickness of the electroplated gold is controlled by the plating time, with the current density fixed at 2 mA/cm^2. The resulting electroplating rate is 0.11 μm/min. To form a 6 μm thick sacrificial layer to realize the standing posts and elevated spans, a thick photo resist (SPR 220-7 [15]) was coated and patterned by means of the UV stepper lithography equipment. The patterned sacrificial layer was thermally cured at 115 °C in order to de-gas the photoresist. After the electroplating step, a titanium-gold layer was coated onto the chip by E-beam metallization. This titanium-gold layer provides electro-contact for the following gold plating step. Next, an additional thick photoresist layer (SPR 220-3 [15]) was spun on and patterned to form a 3 μm thick sacrificial layer. After the photoresist was cured in the oven at a temperature of 120 °C for 5 minutes, 3 μm thick gold was electroplated on to form the spans. Finally, the whole chip was immersed in a photoresist remover solution (NANO Remover PG [15]) at a
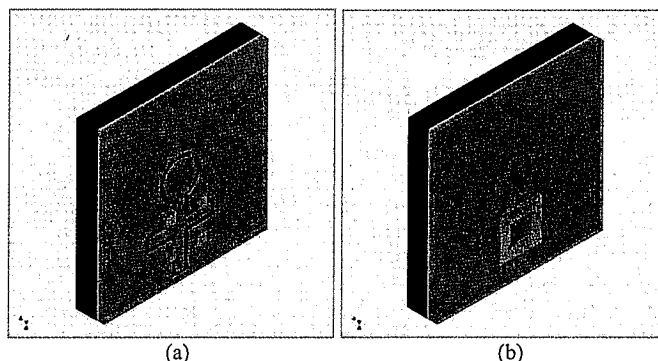

(a)   (b)

Fig. 7. Two gold electroplating steps for constructions of the air-bridge. (a) 4 posts; (b) spans.

temperature of 60 °C in order to remove the photoresist and the excess metal. Ultra-sound agitation may be used to accelerate the lift-off step.

The entire electroplating process was carried out in a Process Systems International (PSI) Excellite 9000 [15] plating bath. Plating cell configurations utilize a rotating wheel (cathode), where one wafer can be attached, along with reciprocating anodes. During plating, as the wafer rotates, the anodes move continuously from left to right and vice versa, and a high precision pulse DC power supply provides rectification. In our setup, the device chip was held on a dummy wafer using purified bee's wax. The bee's wax melts at around 80 °C. Since the electroplating process is performed at 60 °C, the bee's wax provides sufficient adhesion.

Fig. 8. SEM images of a slot-ring device and an air-bridge structure.

IV. RESULTS

The fabrication process described above was first optimized on the test wafer in order to produce a functioning air-bridge structure in the absence of an HEB device. The optimization process resulted in a robust air-bridge structure with a yield of better than 95 %. The resistance between the air-bridge structure and the ground plane on the device substrate was less than 5 Ω. After the evaluation of the air-bridge structure on the test wafer, we proceeded with a working HEB device fabricated on a silicon substrate. Extra care is required when the air-bridge structure is fabricated on an actual HEB device. The yield drops to about 75 %. The HEB devices fabricated on the NbN film exhibited a resistance of 90 to 100 Ω compared with a slot-ring antenna resistance of about 90 Ω. A good resistance match between the slot-ring antenna and the device is highly desirable in order to achieve a good power coupling efficiency.

Scanning electron microscope photographs of the air-bridge integrated slot-ring antenna and an HEB device are shown in Fig. 8. The images were taken on the JEOL 6400 SEM [15] system. Photos (a) and (b) were taken with the sample stage tilted at 45 degrees, while photos (c) and (d) were taken as the stage tilted at 75 degrees. The air-bridge structure appears to be very uniform and robust. This is also verified by the fact that the air-bridge survived the ultra-sound agitation step, known to be very violent and destructive.

V. CONCLUSION

An air-bridge integrated slot-ring antenna has been designed for operation at 1.6 THz. Numerical calculations of the antenna radiation pattern show a narrow beamwidth (~3°) of the slot-ring antenna at the center frequency. From the simulation, the air-bridge integrated stub filter exhibits a good bandstop characteristic with a rejection of 25 dB at the center frequency.

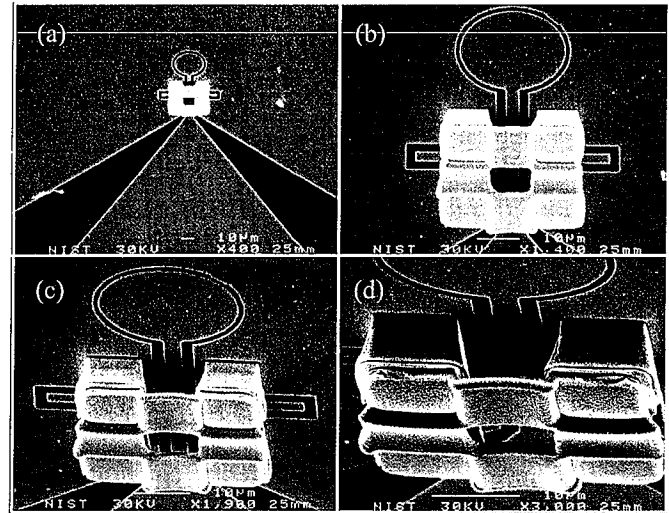We have demonstrated a new fabrication technique for making an air-bridge integrated slot-ring antenna with an HEB device. Further characterization of the HEB device in terms of power coupling and noise temperature measurements is on-going. Future multi-pixel focal plane arrays for terahertz imaging may utilize the quasi-optical configuration demonstrated here.

REFERENCES

[1] S. Wang and X.C. Zhang, "Pulsed terahertz tomography," Journal of Physics D – Applied Physics, vol 37 (4), pp R1-R36, Feb 2004.
[2] R. Hoogeveen, Overview of TELIS system. Available: http://www.sron.nl/www/code/eos/telis/telis.php?1=1&menuID=1127
[3] T. Nagashima, K. Takata, S. Nashima, H. Harima and M. Hangyo, "Measurement of electrical properties of GaN thin films using Terahertz-time domain spectroscopy," Japanese Journal of Applied Physics Part 1, Vol 44 (2), pp 926-931, Feb 2005.
[4] E. Gerecht, et al, " Development of TREND- a low noise receiver user instrument at 1.25 THz to 1.5 THz for AST/RO at the South Pole," 14th Intern. Symp. Space THz Tech., Tucson, AZ, Apr. 2003.
[5] S. Cherednichenko, M. Kroug, H. Merkel, P. Khosropanah, A. Adam, E. Kollberg, D. Loudkov, G. Gol'tsman, B. Voronov, H. Richter, and H.-W. Huebers, "1.6 THz Heterodyne Receiver for the Far Infrared Space Telescope", Physica C, Superconductivity and its Applications, 372-376: pp. 427-431, 2002.
[6] E. R. Mueller, Terahertz radiation: application and sources. Available: http://www.aip.org/tip/INPHFA/vol-9/iss-4/p27.html
[7] J. Faist, et al, "High power mid-infrared (~ 5 μm) quantum cascade lasers operating above room temperature," Applied Physics Letter, Vol 68 (26), pp. 3680-3682, June 1996.
[8] S. Raman and G. M. Rebeiz, "Single- and dual-polarized millimeter-wave slot-ring antennas", IEEE Transaction on Antennas and Propagation, Vol 44 (11), pp 1438-1444, Nov 1996.
[9] C. E. Tong and R. Blundell, "An annular slot antenna on a dielectric half-space," IEEE Transaction on Antennas and Propagation, Vol 42(7), pp 967-974, July 1994.
[10] D. B. Rutledge, D. P. Neikirk and D. P. Kasilignam, "Integrated circuit antennas," Infrared and Millimeter-Waves, Vol 10, K. J. Button, Ed., pp. 1-90, Academic Press, New York, 1983.
[11] X. Zhao, "Integrated Antenna for THz Hot Electron Bolometer Mixers", Master Thesis, Electrical and Computer Engineering, University of Massachusetts Amherst, Feb. 2005.

[12] E. Gerecht, D. Gu, X. Zhao, J. Nicholson, F. Rodriguez-Morales, and S. Yngvesson, "Development of NbN terahertz HEB mixers coupled through slot-ring antennas," 15th Intern. Symp. Space THz Technology, Northampton, MA, Apr. 2004.

[13] C. A. Balanis, Antenna Theory – analysis and design, 2nd edition, John Wiley & Sons, Inc. 1997.

[14] D. F. Filipovic, S. S. Gearhart, and G. M. Rebeiz, " Double-slot antennas on extended hemispherical and elliptical silicon dielectric lenses," IEEE Transaction on Microwave Theory and Technology, vol 41, pp 1738-1749, Oct. 1993.

[15] Products and companies named here are cited only in the interest of complete scientific description, and neither constitute nor imply endorsement by NIST or by the US government. Other products may be found to serve just as well.